catalysts

MDPI

Article

High-Temperature Abatement of N_2O over $FeOx/CeO_2$-Al_2O_3 Catalysts: The Effects of Oxygen Mobility

Larisa Pinaeva [1], Igor Prosvirin [1], Yuriy Chesalov [1] and Victor Atuchin [2,3,4,5,*]

1 Boreskov Institute of Catalysis SB-RAS, 5, Lavrentiev ave, Novosibirsk 630090, Russia
2 Laboratory of Optical Materials and Structures, Institute of Semiconductor Physics, SB-RAS, Novosibirsk 630090, Russia
3 Research and Development Department, Kemerovo State University, Kemerovo 650000, Russia
4 Department of Industrial Machinery Design, Novosibirsk State Technical University, Novosibirsk 630073, Russia
5 R&D Center "Advanced Electronic Technologies", Tomsk State University, Tomsk 634034, Russia
* Correspondence: atuchin@isp.nsc.ru

Abstract: CeO_2-Al_2O_3 oxides prepared by co-precipitation (Ce+Al) or CeOx precipitation onto Al_2O_3 (Ce/Al) to obtain dispersed CeO_2 and samples with further supported FeOx (2.5–9.9 weight% in terms of Fe) were characterized by XRD, XPS, DDPA and Raman. Fe/Ce/Al samples with lower surface concentrations of Fe^{3+} were substantially more active in N_2O decomposition at 700–900 °C. It was related to higher oxygen mobility, as estimated from $^{16}O/^{18}O$ exchange experiments and provided by preferential exposing of (Fe-)Ce oxides. Stabilization of some Ce as isolated Ce^{3+} in Fe-Ce-Al mixed oxides dominating in the bulk and surface layers of Fe/(Ce + Al) samples retards the steps responsible for fast additional oxygen transfer to the sites of O_2 desorption.

Keywords: N_2O decomposition; Fe-Ce-Al mixed oxide; oxygen mobility

check for updates

Citation: Pinaeva, L.; Prosvirin, I.; Chesalov, Y.; Atuchin, V. High-Temperature Abatement of N_2O over $FeOx/CeO_2$-Al_2O_3 Catalysts: The Effects of Oxygen Mobility. *Catalysts* **2022**, *12*, 938. https://doi.org/10.3390/catal12090938

Academic Editors: Gassan Hodaifa and Rafael Borja

Received: 4 August 2022
Accepted: 22 August 2022
Published: 24 August 2022

1. Introduction

Nitric acid is a key chemical with annual production at above 65 million tons mainly driven by the fertilizer industry. Nitrous oxide (N_2O) is produced as an unwanted, but inevitable by-product at HNO_3 industrial manufacture by ammonia oxidation. Its emissions by nitric acid plants are growing from 5 to 12 kg N_2O/ton HNO_3 according to the tendency to high-pressure processes [1]. Meanwhile, nitrous oxide is a potent greenhouse gas characterized by about 300 times the Global Warming Potential of CO_2 and contributes to the greenhouse effect and ozone layer depletion. Therefore, 330–780 thousand tons of N_2O annually emitted at HNO_3 production are equivalent to 100–240 million tons/y CO_2e. It can be deleted by placing the catalysts in several points of the ammonia processing flowsheet [2], including that immediately downstream the Pt–Rh gauzes operating at 800–900 °C. A tendency of recent years to increase weight space velocity and reduce the charge of platinum-group metals in the reactor increased the risk of ammonia slipping at gauze ageing or damage. Therefore, efficient conversion of NH_3 to NO + NO_2, while N_2O is low is one of the necessary features for N_2O decomposition catalysts operating in these conditions as well.

Fe-Al-O-based catalytic compositions are efficient both in selective ammonia oxidation to NO and NO_2 [3–5] and in selective N_2O decomposition under the conditions of the nitric acid plant [4–8] without decrease in NOx yield [6,7]. The activity in both reactions was shown to increase by using CeO_2 as the support instead of alumina [4]. It was due to the appearance of the additional pathway of the oxygen supply through oxygen vacancies located in the near subsurface layers of ceria to Fe active sites facilitating the rate-determining step of O_2 desorption. An increase in both ceria and $Co(Fe)O_x$ dispersion could additionally promote oxygen diffusion to Fe. In the first case it is because both

distributions of oxygen vacancies and oxygen storage and release capability of CeO_2 are related to its particle size [9,10]. The positive effect of the dispersion of Co oxide spinel phase [11,12] or FeOx species over ceria and alumina [4,5,8] onto activity in both reactions was already shown and related to enhanced oxygen diffusion through the active component/support interface periphery [4,11,12]. However, for individual CeO_2 all positive effects resulting from fast oxygen transfer are restricted by its low surface area under the reaction conditions [10]. Several methods to stabilize dispersed CeO_2 particles over Al_2O_3 after calcination at above 800 °C were reported. They include the sol–gel method using aluminum tri-sec-butoxide and Ce(III) nitrates as precursors [13], impregnation of alumina with an aqueous solution of $(NH_4)_2[Ce(NO_3)_6]$ [14] or stabilization of a complex of the CeO_2 precursor in a homogeneous polymeric matrix (Pechini route) followed by supporting onto alumina [15,16].

In the current study, we used CeO_2 precipitation onto Al_2O_3 or CeO_2 and Al_2O_3 co-precipitation methods to increase CeO_2 dispersion in the final supports compared with individual CeO_2. The reasons for the principally different activity of FeOx/CeO_2-Al_2O_3 samples prepared using these supports have been elucidated.

2. Results and Discussion

2.1. Phase Composition (XRD)

XRD patterns of Ce/Al and (Ce + Al) samples revealed a mixture of CeO_2, θ-Al_2O_3 and γ-Al_2O_3, phases (Figure S1 in Supplementary Materials). Lattice parameters of CeO_2 in both samples were exactly the same (Table 1) and practically coincided with those for pure CeO_2 calcined at 900 °C (a = b = c = 5.412 Å), while the values of coherent scattering area d_{XRD} calculated by the Scherrer equation were lower (40 and 11 nm for Ce/Al and (Ce + Al), respectively, compared with 68 nm for pure CeO_2 [4]). Lattice parameters of γ(+θ)-Al_2O_3 phases cannot be calculated correctly because of low intensity and substantial broadening of corresponding overlapping signals. Therefore, some penetration of Ce ions into their lattices cannot be excluded. At the same time, higher dispersion of alumina species in the (Ce + Al) sample follows from larger widths of the peaks at 45.5° and 67.0° (Figure S1).

Table 1. Structural characteristics of Ce/Al and (Ce + Al) based samples.

Sample	S_{BET} (m^2g^{-1})	Phase Composition (Lattice Parameters)	D_{XRD} (nm)
Ce/Al	63	CeO_2 (a = b = c = 5.411 Å)	40
		(θ + γ)-Al_2O_3	-
3.8 Fe/Ce/Al	50	CeO_2 (a = b = c = 5.411 Å)	41
		(θ + γ)-Al_2O_3	-
9.9 Fe/Ce/Al	35	CeO_2 (a = b = c = 5.411 Å)	46
		(θ + γ)-Al_2O_3	-
		α-Fe_2O_3 (a = b = 5.035 Å, c = 13.741 Å)	32
(Ce + Al)	94	CeO_2 (a = b = c = 5.411 Å)	11
		(θ + γ)-Al_2O_3	tr.
2.5 Fe/(Ce + Al)	70	CeO_2 (a = b = c = 5.411 Å)	12
		(θ + γ)-Al_2O_3	tr.
6.6 Fe/(Ce + Al)	58	CeO_2 (a = b = c = 5.411 Å)	14
		(θ + γ)-Al_2O_3	tr.
		α-Fe_2O_3 (a = b = 5.035Å, c = 13.741 Å)	39

Fe deposition resulted in a decrease in S_{BET} value and a consistent increase in D_{XRD} of CeO_2 species; the value of effect depended on the quantity of Fe (Table 1). Although CeO_2 lattice parameters did not change for all Fe content ranges, the formation of Fe-Ce-O solid solution cannot be excluded. Ceria lattice shrinkage was measured in Au/Ce-Fe-O (Ce/Fe = 9) [17], Fe/CeO_2 (Ce/Fe = 4–9) [18] or CeO_2–Fe_2O_3 (Ce/Fe = 2.3) [19] samples prepared by procedures favoring homogeneous distribution of Fe and Ce in the samples

before their high temperature treatment. It was due to the replacement of Ce^{4+} ions in the typical cubic fluorite lattice (radius 0.097–0.101 nm) by Fe^{3+} ions (0.049–0.078 nm, depending on coordination and spin state). However, at smaller Fe content in $Fe_xCe_{1-x}O_2$ ($x \leq 0.05$, or Ce/Fe $\geq$ 20) even a slight increase in lattice parameter compared with pure CeO_2 was observed [18] and related to partial Ce^{4+} reduction to the larger (0.123 nm) Ce^{3+} ion [20]. Although in our case Ce/Fe ratio varies within 1.1–6.2, these differently directed effects could compensate for each other because Fe was supported onto support already calcined at 900 °C diminishing the efficiency of its incorporation into CeO_2 lattice, while incorporation of some Fe cations into the alumina component is possible as well.

Nevertheless, neither relative intensity and dispersion of γ-,θ-Al_2O_3 changed (Figure S1, inserts), nor α-Al_2O_3 appeared in both Fe/Ce/Al and Fe/(Ce+Al) samples (Figure S1), unlike Fe/Al_2O_3 samples with reasonably close S_{BET} and Fe content values [4]. Hence, the formation of Fe-Al-O solid solutions in Ce-containing samples is hardly ever possible.

2.2. Catalytic Activity in N_2O Decomposition and NH_3 Oxidation

The activity of Ce/Al and (Ce + Al) based catalysts expressed in terms of N_2O conversion at 800 °C versus Fe content (Figure 1A) is typical for temperature range 700–900 °C (Figure S2). For every type of support, it increases with Fe content. O_2 and H_2O expectedly retard the reaction (Figure S3). Conversion values measured for Fe/(Ce + Al) samples are evidently lower than for Fe/Ce/Al. Therefore, better dispersion of CeO_2 species at close Ce content in the sample does not guarantee higher activity even at higher S_{BET} values (Table 1).

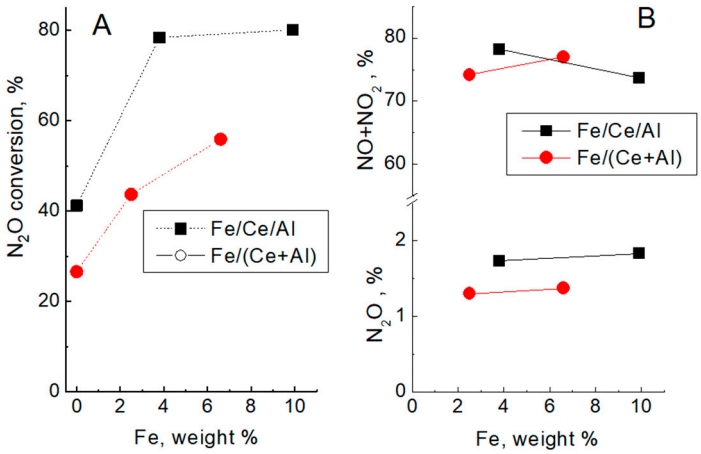

Figure 1. Dependence of N_2O conversion (**A**) and (NO + NO_2) and N_2O yield at NH_3 oxidation (**B**) on Fe content at 800 °C for Ce/Al and (Ce + Al) based samples.

For all samples, the conversion of NH_3 and yield of (NO + NO_2) (Y_{NO+NO2}) increase, while that of N_2O (Y_{N2O}) decreases with temperature; Y_{NO+NO2} = 74–80% and Y_{N2O} = 0.5–1.8% at T $\geq$ 800 °C (Figure S4A,B, and Figure 1B). High stability for 8 h of operation, at least, was shown as well (Figure S4C). We estimated that at an NH_3 slip of 1% (although such a value is practically impossible) the increment of N_2O concentration after the Fe-Ce-Al catalyst at 800 °C will be 65–90 ppm. At the average N_2O concentration downstream of the fresh gauzes of 1500 ppm [2], such an addition will diminish N_2O conversion only by 4–6%.

2.3. Microstructure and Morphology

2.3.1. DDPA

Detailed analysis of dissolution kinetics of Fe, Ce and Al in different samples has been presented in corresponding section of Supporting Information. Herein, we summarized and discussed the main facts that are important for understanding the composition and spatial distribution of different compounds in Fe/(Ce + Al) and Fe/Ce/Al samples.

Mixed oxides of different compositions dissolving consecutively in either HCl or HF (Figure S6) represent most of the 2.5 Fe/(Ce + Al) sample (Table 2). The most abundant compound is Fe-Ce-Al mixed oxide with $Fe_{0.03}Ce_{0.09}Al$ stoichiometry which (Figure 2A): encapsulates the particles of Fe-Ce mixed oxide ($Fe_{0.02}Ce$ stoichiometry); is partially screened by more disordered Fe-Ce-Al mixed oxide with higher content of Fe and Ce ($Fe_{0.05}Ce_{0.26}Al$ stoichiometry) and Fe-Al-O compounds dissolving in HCl.

Table 2. Stoichiometry/quantity (mmol/g, without account of for O) of compounds dissolved in HCl and HF flows in different samples. Quantities of insoluble Ce compounds were calculated from balance equations.

Sample	Ce + Al	2.5 Fe/(Ce + Al)	3.8 Fe/Ce/Al
HCl	Al/1.15	Fe/0.06	Fe/0.07
		$Fe_{0.05}Al$/1.30	$Fe_{0.29}Al$/0.37
	$Ce_{0.05}Al$/0.67	$Fe_{0.05}Ce_{0.26}Al$/0.65	$Fe_{0.19}Ce$/0.12
HF	$Ce_{0.05}Al$/7.92	$Fe_{0.05}Ce_{0.26}Al$/2.62	Fe/0.03
	Al/0.45	$Fe_{0.03}Ce_{0.09}Al$/8.14	$Fe_{0.08}Ce_{0.2}Al$/2.93
	Ce/0.069	$Fe_{0.02}Ce$/0.80	$Fe_{0.04}Al$/7.47
Insoluble Ce	2.4	0.7	2.0

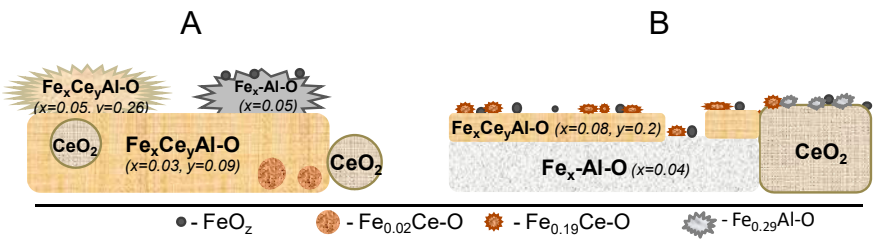

Figure 2. Structures formed in 2.5 Fe/(Ce + Al) (**A**) and 3.8 Fe/Ce/Al (**B**) samples.

The decreasing Fe/Al ratio in Fe-Al-O compounds points to the formation of mixed oxide with most disordered near-surface layers enriched by Fe^{n+} (Figure S6B). At the same time, the protocol of Fe supporting includes using of acidic solutions giving rise to the dissolution of some poorly crystallized alumina detected in the initial support (Figure S5A, Table 2). In this case, the formation of a γ-$FeAlO_3$-like compound with spinel structure is quite possible after following drying and calcination at T < 400 °C [21]. Since the mutual Fe_2O_3 and Al_2O_3 solubility in such structure decreased prominently with calcination temperature rise, its decomposition could happen in our case as well leading to the formation of highly dispersed FeO_x species (0.06 mmol/g) on the surface of Fe-Al mixed oxide with $Fe_{0.05}Al$ stoichiometry. Its quantity (1.3 mmole/g) is reasonably close to that of alumina dissolving in HCl in the initial support (1.15 mmole/g) (Table 2). Calculation showed that identified soluble compounds include all Al and Fe in the sample, while about 0.7 mmol/g of Ce, or 25% of its general content in the sample, represent insoluble oxides (Table S1 in Supplementary Materials, Table 2) which are, more probably, small sized CeO_2 species with unmodified fluorite lattice (Table 1). Their spatial location in the sample is not clear, but encapsulation by Ce-Al mixed oxide preventing Fe incorporation into the lattice is quite reasonable because the same was detected for the particles of Fe-Ce mixed oxide.

The overall quantity of soluble Ce-containing compounds in the 3.8 Fe/Ce/Al sample is substantially lower as compared with the 2.5 Fe/(Ce + A) sample (Table 2), which can be related to a larger size of CeO_2 particles (Table 1). Most of the dissolved part of the sample is represented by Fe-Al mixed oxide partially screened by Fe-Ce-Al one with $Fe_{0.04}Al$ and $Fe_{0.08}Ce_{0.2}Al$ stoichiometries, correspondingly (Figure S7C and Figure 2B, Table 2). Surface layers are composed of more dispersed/disordered binary Fe-Al and Fe-Ce oxides and some FeOx dissolved in HCl (Figure S7, Table 2). Completely independent kinetics of their dissolution can be in the case dispersed FeOx species are located on the surface of any of binary oxides and even non-dissolved large CeO_2 species with unmodified fluorite lattice

including 2.0 mmol/g of Ce, or more than 70% of its content in the sample (Figure 2B, Table 2). A substantially higher quantity of Fe in the surface located Fe-Al-O compounds ($Fe_{0.29}Al$ stoichiometry) compared with that in 2.5 Fe/(Ce + Al) could be due to other mechanisms of their formation compared with that in 2.5 Fe/(Ce + Al) sample (see below).

2.3.2. Raman

The band at 462.9 cm^{-1} in the FT-Raman spectra of Ce/Al sample (Figure 3A) is typical for the F_{2g} vibration mode of the fluorite structure of CeO_2 [22,23]. Its width at ~24.5 cm^{-1} (Table 3) should correspond to a size of CeO_2 species at about 10 nm [23,24] which is substantially less than the estimated value of D_{XRD} at 40 nm (Table 1). At the same time, the particles of 10 nm in a size should be characterized by the Raman band at ~448 cm^{-1}, as follows from experimental dependence obtained for CeO_2 and CeO_2-Al_2O_3 composites [15]. Spanier et al. [24] showed that lattice strains in the smaller nanoparticles have the largest contribution to both Raman peak position shift and its broadening compared with other reasons (phonon confinement, particle size distribution, defects, phonon relaxation). Tsunekawa et al. [25] attributed the formation of additional strains to the reduction of Ce^{4+} ions to Ce^{3+} ions caused by an increasing molar fraction of oxygen vacancies. We supposed that in our case stabilization of additional Ce^{3+} within fluorite lattice and appearance of strains can be due to insertion of lower sized Al^{3+} cations into the interstitial sites of c-CeO_2 lattice resulting in charge redistribution, such as observed in c-CeO_2/α-Al_2O_3 composites with close Ce/Al ratio [26]. The intensity of the CeO_2 band in the spectra of Fe/Ce/Al samples does not decrease prominently (Table 3), while its position and especially the width become very close to those in the single crystals [23]. Such changes could be due to better ordering of CeO_2 structure resulting from Al^{3+} "extraction" from the lattice after impregnation by acidic Fe-containing solutions that proceed with temperature increase and, to a less extent, some enlargement of crystallized CeO_2 species (Table 1). It is the stabilization of small Fe-Al-O clusters in the points of Al insertion into CeO_2 lattice after their extraction, but not γ-$FeAlO_3$ phase decomposing at T > 400 °C, that can be responsible for the substantially higher content of Fe in the Fe-Al mixed oxide ($Fe_{0.29}Al$) identified by DDPA compared with that in 2.5 Fe/(Ce + Al) sample (Table 2). Bands at 231 (not shown), 301, 419 and 622 cm^{-1} in the spectrum of 9.9 Fe/Ce/Al sample are usually related to lattice vibrations in α-Fe_2O_3 which agrees with XRD data (Table 1).

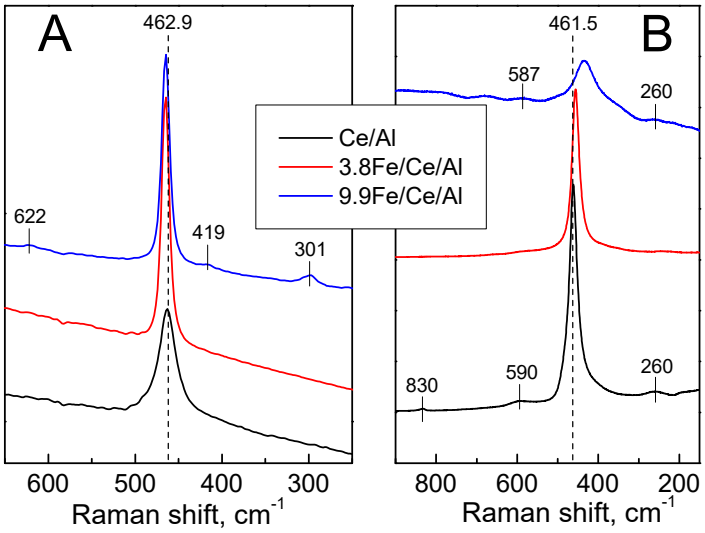

Figure 3. FT-Raman (**A**) and Raman (**B**) spectra of Ce/Al-based samples.

Table 3. Position, width (FWHM) and integral intensity of F_{2g} vibrational mode of CeO_2 in the FTRaman and Raman spectra.

Sample	Position, cm^{-1}		FWHM, cm^{-1}		Integral Intensity, arb.unit	
	FT-Raman	Raman	FT-Raman	Raman	FT-Raman	Raman
Ce/Al	462.9	461.5	24.5	21.2	0.101	30399
3.8 Fe/Ce/Al	465.1	455.8	10.6	21.8	0.087	27805
9.9 Fe/Ce/Al	464.9	433.0	10.8	66.3	0.079	26155
Ce + Al	464.1	462.7	18.3	17.0	0.219	266717
2.5 Fe/(Ce + Al)	464.0	455.8	17.3	23.4	0.0895	34159
6.6 Fe/(Ce + Al)	464.0	459.6	16.3	20.0	0.0327	19715

The absence of the band at ~377 cm^{-1} related to α-Al_2O_3 phases [27] in the Raman spectra giving information on near subsurface layers of all Ce/Al-based samples (Figure 3B) agrees with XRD and DDPA data. F_{2g} mode of CeO_2 at 461.5 cm^{-1} in the spectrum of support is supplemented by the bands at ~590, ~260 and ~830 cm^{-1} ascribed to the vacancy-interstitial (Frenkel-type) oxygen defects, surface mode, and peroxide (O_2^{2-}) stretching vibration at the defective ceria surfaces, respectively [28–30]. These bands disappear in the spectrum of the 3.8 Fe/Ce/Al sample because the doping element can annihilate oxygen defects by dopant interstitial compensation mechanism [31]. The low-frequency shift of the CeO_2 band and its broadening (Table 3) typical for smaller particles was detected in the spectra of Fe/Ce/Al samples which contradicts the slight increase in averaged sizes of crystalline CeO_2 particles (Table 1). Therefore, the formation of highly dispersed particles of Fe-Ce mixed oxide in the surface layers of the 3.8 Fe/Ce/Al samples was detected by DDPA (Table 2) with inhomogeneous strains due to Ce^{3+} ions therein [15,28] can be responsible for such changes. Asymmetrical broadening with a low-energy shoulder of CeO_2 band, especially prominent in the 9.9 Fe/Ce/Al sample, can result from a higher concentration of such compounds or higher content of α-Fe_2O_3 therein. In line with this, bands at ~260 and ~590 cm^{-1} appear again.

The band at 464 cm^{-1} which is responsible for F_{2g} mode of fluorite lattice attenuates drastically in Fe/(Ce + Al) samples compared with that in the initial support (Figure 4A, Table 3). It is, more probably, due to the noticeable additional inclusion of Ce into alumina or Ce-Al mixed oxides with low Ce content where it exists preferentially as isolated Ce^{3+} ions in the presence of Fe. Indeed, Ce/Al = 0.05 in Ce-Al mixed oxide detected by DDPA in the (Ce + Al) sample but increased up to 0.09–0.26 after Fe supporting (Table 2). The absolute value of mixed oxides increased as well, while the quantity of insoluble CeO_2 decreased from 2.4 mmol/g to 0.7 mmol/g (Table 2). At the same time, the position of CeO_2 F_{2g} mode in Fe/(Ce + Al) samples changed non-substantially pointing to the absence or low degree of ceria lattice modification by foreign atoms compared with the support. In this case, a slightly higher FWHM compared with that in Fe/Ce/Al samples is due to the particle size effect, which is true for crystallized particles, at least (Table 1) [15].

The band at ~377 cm^{-1} related to α-Al_2O_3 phases [27] was absent in the Raman spectra of near subsurface layers of (Ce + Al) based samples as well which agrees with XRD data (Figure S1, Table 1). After iron supporting, they undergo changes that are very similar to those in the bulk of the sample (Figure 4B, Table 3). An even more prominent drop in the intensity of the Ce band compared with that for the bulk can be related to the additional formation of Fe-Ce-Al mixed oxide with high Ce content ($Fe_{0.05}Ce_{0.26}Al$ stoichiometry) (Table 2). Nevertheless, the close CeO_2 band position and FWHM values in FT-Raman and Raman spectra point to a more uniform distribution of elements in the bulk and surface layers of these samples as compared to those in Ce/Al-based samples. This agrees with DDPA data on the preferential formation of Fe-Ce-Al-O mixed oxides in the 2.5 Fe/(Ce + Al) sample, while obviously spatially divided Fe-Al-O, Fe-Ce-O and more CeO_2 were found in the 3.8 Fe/Ce/Al sample.

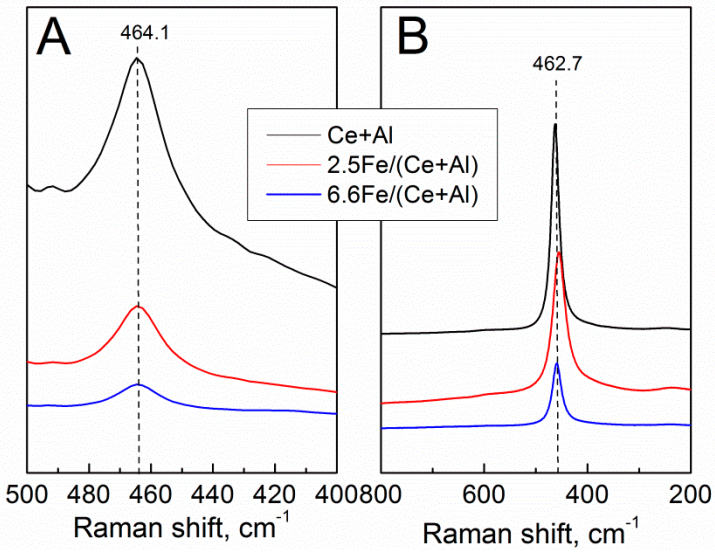

Figure 4. FT-Raman (**A**) and Raman (**B**) spectra of (Ce + Al) based samples.

2.4. Surface Composition (XPS)

The normal complex formed due to shake-down satellites from an O1s to Ce 4f electron transfer in the Ce 3d spectra of all CeO_2 containing samples (Figure 5A) was supplemented by the features marked as v′ and u′ due to the presence of Ce^{3+} [10]. An increase in Ce^{3+} fraction from 8% of total surface Ce concentration in CeO_2 (spectrum not shown for shortness) up to 20% in 0.86 Fe/CeO_2 sample was related to the formation of Fe-Ce–O solid solution or Fe-Ce mixed oxide [4,32]. Similar compounds of $Fe_{0.19}Ce$ stoichiometry have been detected in the 3.8 Fe/Ce/Al sample (Table 2, Figure 2). Therefore, there are two reasons that explain the further increase in Ce^{3+} fraction in 3.8 Fe/Ce/Al (25%) and especially Fe/(Ce + Al) (31-33%) samples (Table 4): stabilization of both isolated Ce cations in alumina-based structure of Fe-Ce-Al mixed oxides (Table 2) and Ce located on CeOx-AlOx boundary in the same oxides as Ce^{3+}; lower CeO_2 particle sizes (12 nm (2.5 Fe/(Ce + Al)) and 41 nm (3.8 Fe/Ce/Al), Table 1) compared with that in Fe/CeO_2 (55 nm [4]) favoring reduction in Ce^{4+} [25].

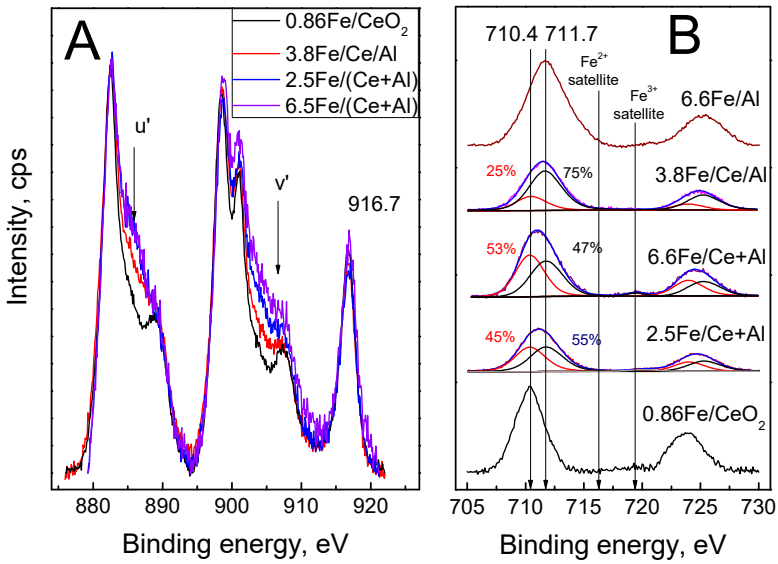

Figure 5. Ce 3d (**A**) Fe 2p (**B**) spectra of Fe-Ce-Al-O samples including contributions of Fe_2O_3 (710.4 eV) and FeOOH (711.7 eV)-like structures to overall Fe2p spectrum. 6.6 Fe/Al_2O_3 and 0.86 Fe/CeO_2 samples were studied by Pinaeva et al. [4].

Table 4. Surface (XPS) composition of different Fe-Ce-Al-O samples.

Sample	Ce^{3+}, % of Total	Ce_s, [a] at. %	Ce_{exp}, rel.units [b]	Ce/Al	Fe_s [a] at. % [a]	Fe_{exp}, rel.units [b]
3.8 Fe/Ce/Al	25	3.7	184	0.12	1.6	80
2.5 Fe/(Ce + Al)	31	2.4	171	0.075	1.7	117
6.6 Fe/(Ce + Al)	33	2.7	159	0.096	2.7	166

[a]: calculated supposing C-containing compounds are absent under reaction conditions; accounting of C does not change the order of values. [b]: calculated as $Fe(Ce)_{exp} = Fe(Ce)_s \cdot SSA$.

Surface Ce concentration (Ce_s) and Ce/Al ratios in all samples (Table 4) are substantially lower than should follow from its integral composition (Ce/Al ≈ 0.3, Table S1), which agrees in general with higher dispersion of Al-containing compounds. The highest Ce_s and Ce/Al values were measured in the 3.8 Fe/Ce/Al sample (Table 2). However, the concentration of exposed Ce (Ce_{exp}) in the Fe/Ce/Al and Fe/(Ce + Al) samples differ not so prominently because of higher S_{BET} values in the last (Table 1). It is problematic to estimate Ce_s in the Fe-Ce-Al-O compounds of the samples. This value should be slightly higher in 2.5 Fe/(Ce + Al) sample (Ce/Al = 0.26 instead of Ce/Al = 0.2 for 3.8 Fe/Ce/Al sample, Table 2). Surface areas of crystallized CeO_2 particles in Fe/(Ce + Al) and Fe/Ce/Al samples as formally estimated from their absolute content (Table S1) and sizes (Table 1) are quite close. However, encapsulation of about 29% of Ce composing Fe-Ce-O mixed oxides (Fe/Ce = 0.02, 0.8 mmol/g, Table 2) by Fe-Ce-Al mixed oxide was found for 2.5 Fe/(Ce + Al) sample (Figure 2A). This allows supposing bulk location of some CeO_2 species as well thus decreasing Ce_s value therein. In addition, preferential exposing of highly dispersed Fe-Ce-O compound with $Fe_{0.19}Ce$ stoichiometry can additionally contribute to higher Ce_s value in the 3.8 Fe/Ce/Al sample. Hence, a substantial part of Ce_s in the Fe/(Ce + Al) samples composes Fe-Ce-Al mixed oxides with a high concentration of Ce^+, while the fraction of CeO_2-like structures is higher and seems to be responsible for greater Ce_s value in Fe/Ce/Al samples.

The 3.8 Fe/Ce/Al sample is characterized by the lowest Fe surface concentration (Fe_s) and the quantity of exposed Fe as related to a weight unit (Fe_{exp}) (Table 4). BE values of the $Fe2p_{3/2}$ spectra ranging from 710.9 eV to 711.7 eV (Figure 5B) evidence presence of Fe^{3+} in oxyhydroxide environment (like in α- or γ-FeOOH), and in the oxide (like Fe_2O_3) structures [33–35], correspondingly dominating in 6.6 Fe/Al_2O_3 and 0.86 Fe/CeO_2 samples [4]. Although the positions of the Fe $2P_{3/2}$ peak for Fe^{2+} in $Fe_{0.94}O$, $2FeO \cdot SiO_2$ or $Fe_{0.01}Mg_{0.99}O(100)$ single crystal were characterized by the values between 709.0 and 710.4 eV, its absence or low content in our samples follows from the absence of distinct satellite at 714.6–716 eV [36,37]. FeOOH usually undergoes a dehydroxylation reaction at 250–300 °C resulting in Fe_2O_3 [38]. At the same time, tetrahedral Fe^{3+} cations coordinating both terminal and bridging OH groups were found on the surface of both Fe-Al-O solid solution and highly dispersed FeO_x species resulting from the decomposition of γ-$FeAlO_3$–like structures [21]. In accordance with this, the $Fe2p_{3/2}$ band at 711.7 eV (dominates in 3.8 Fe/Ce/Al sample) can be subscribed to: Fe^{3+} ions in Fe-Al mixed oxides, including those with $Fe_{0.29}Al$ stoichiometry (Table 2) formed by "extraction" of Al from CeO_2 lattice after Fe supporting; highly dispersed FeOx species resulted from the decomposition of Fe-Al-O.

The band at 710.4 eV can characterize FeOx species on the surface of CeO_2 or Fe^{3+} ions in the Fe-Ce-O compounds (Table 2, Figure 2). Its high abundance in Fe/(Ce + Al) samples (45–53% of total Fe_s) contradicts lower Ce_s values compared with that in 3.8 Fe/Ce/Al sample. However, the substantial part of the surface Fe in Fe/(Ce + Al) samples composes Fe-Ce-Al mixed oxides with reasonably high Ce content (Ce/Al = 0.26, Table 2). It resulted from the inclusion of additional Ce from CeO_2 into the surface layers of alumina or Ce-Al mixed oxide of the initial support with Fe participation. Therefore, preferential formation of Fe-Ce-O oxide-like compounds is quite possible in Fe-Ce-Al mixed oxides. The contribution of Fe-Ce-Al mixed oxides into the surface composition in the 3.8 Fe/Ce/Al sample is not high which follows from the preferential dissolution of FeOx, binary Fe-Al-O and Fe-Ce-O

compounds in HCl (Table 2) and substantially less prominent decrease in integral intensity of F_{2g} vibrational mode of CeO_2 in the near-surface layers of Fe/Ce/Al samples compared with corresponding support (Table 3).

2.5. O_2 Adsorption/Desorption

O_2 transients recorded during the He/0.5 vol.% O_2 switch following 60 s stay in He flow revealed the delay of O_2 response compared with Ar (Figure 6) corresponding to adsorption of reasonably close quantities of oxygen (3×10^{19}–5×10^{19} oxygen atom/g) by reduced sites in the 2.5 Fe/(Ce + Al) and 3.8 Fe/Ce/Al samples.

Differently paired Fe^{2+} and Ce^{3+} ions resulting from the reduction in the oxygen absence are the most evident sites for O_2 dissociative adsorption as coordinatively unsaturated surface metal cations. They can form in the surface layers of FeO_x clusters, including those resulted from the decomposition of α-$FeAlO_3$; Fe-Al-O mixed oxide of $Fe_{0.29}Al$ stoichiometry formed in 3.8 Fe/Ce/Al sample by Al "extraction" from CeO_2 lattice during calcination; highly dispersed Fe-Ce mixed oxides ($Fe_{0.19}Ce$ stoichiometry (Table 2); Fe-Al-Ce-O mixed oxides with high Ce content ($Fe_{0.05}Ce_{0.26}Al$ or $Fe_{0.08}Ce_{0.2}Al$ stoichiometry).

Reduction of isolated Fe^{3+} in the Fe-Al-(Ce-)O mixed oxides with of $Fe_{0.03}Ce_{0.09}Al$ stoichiometry (most of Ce stabilized as Ce^{3+} and unlikely can participate in any redox processes) requires transport of second oxygen atom through the occasional vacancies on the surface or in the bulk of alumina and thus be slow.

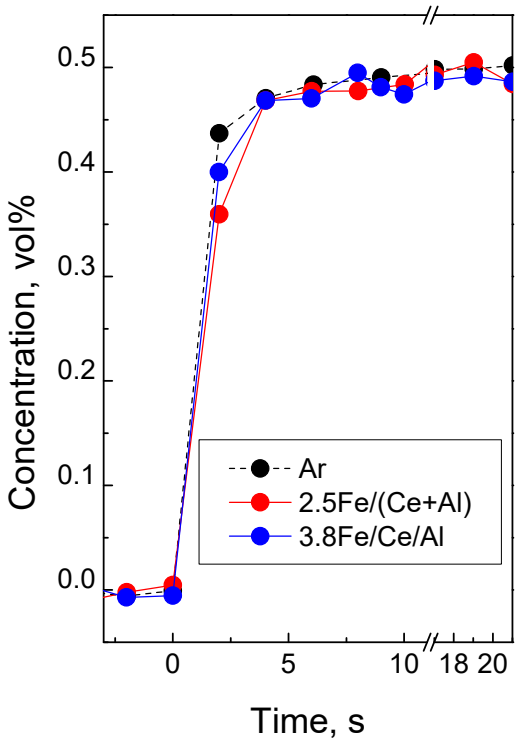

Figure 6. Responses of O_2 and inert label (Ar) during the switch from He to He + 0.5 vol.% O_2 flow over different samples. T = 800 °C.

2.6. Oxygen Mobility (^{18}O SSITKA)

The rates of oxygen exchange in Fe/Ce-Al-O samples in the period of 0–60 s after the $^{16}O/^{18}O$ switch can be ordered as 3.8 Fe/Ce/Al > 6.6 Fe/(Ce + Al)>2.5 Fe/(Ce + Al), as follows from the slope of $N_O(t)/g$ dependencies (Figure 7A). It does not correlate with S_{BET} values of the samples (Table 1) and Fe_s or Fe_{exp} values (Table 4). Moreover, the difference between 3.8 Fe/Ce/Al and Fe/(Ce + Al) samples becomes even more prominent when related to one surface Fe site (Figure 7B). Fast exchange proceeding with reasonably close to initial rate value in these samples during about 20–25 s includes a higher quantity of

oxygen atoms ($N_O = 1 \times 10^{21}$–2×10^{21} O atoms/g) than can be related to Fe, even with an account of that located in the bulk (~1.0×10^{21} O atoms/g in the 6.6 Fe/(Ce + Al) sample with the highest Fe content). Therefore, efficient exchange in the near-surface layers of Ce-containing compounds contributes to N_O as well. Indeed, substantially more profound and faster oxygen exchange took place in Fe/CeO_2 samples compared with Fe/Al_2O_3 [4]. However, both Ce content and Ce_{exp} values are reasonably close in all samples (Table 4). We consider that the higher rate of exchange in the 3.8 Fe/Ce/Al sample can be due to preferential exposure of Fe-Ce mixed oxide or crystallized CeO_2, including that bonded with clusters of FeOx or Fe-Al mixed oxides, while in 2.5 Fe/(Ce + Al) sample substantial part of Fe and Ce are included as preferentially isolated ions into Fe-Ce-Al mixed oxides that still retain alumina-like structure. Although Fe-Ce mixed oxide was detected in the 2.5 Fe/(Ce + Al) sample (Table 2, Figure S6), it obviously locates in bulk (Figure 2), like part of CeO_2, and thus does not contribute to the fast oxygen exchange.

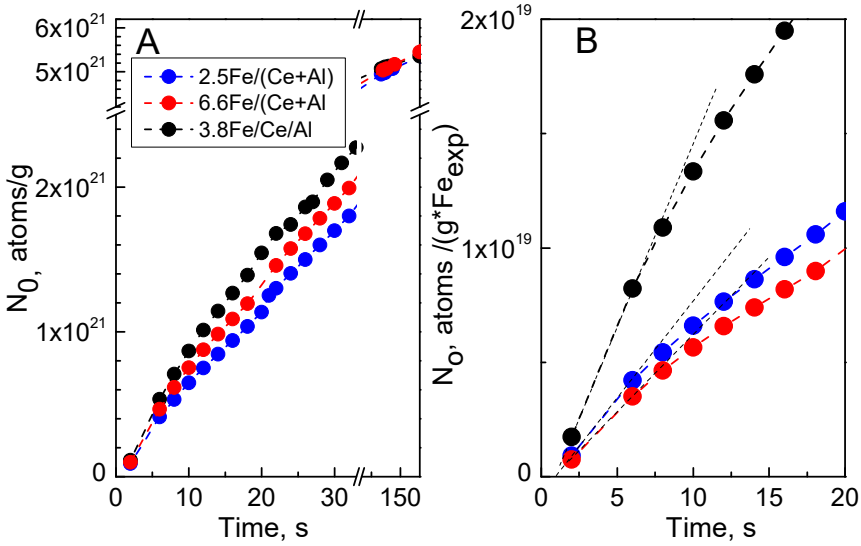

Figure 7. Time dependencies of the quantity of exchanged oxygen (No) as related to weight unit (**A**) or one surface Fe site (**B**) in ^{18}O SSITKA experiments for different samples. T = 800 °C.

2.7. Discussion

In accordance with the simplified redox scheme of N_2O decomposition proposed by Kapteijn et al. [39]:

$$N_2O + * \rightarrow N_2 + O^*$$

$$2O^* \leftrightarrow 2^* + O_2$$

one active (reduced) site is sufficient for N_2 to evolve, but two neighboring O* are necessary for the desorption of O_2. Factually, two neighboring active sites for N_2O adsorption are desired for efficient reaction running, especially provided oxygen desorption from the surface is the rate-controlling step of this reaction [39]. Potential quantities of such reduced sites under reaction conditions in 2.5 Fe/(Ce + Al) and 3.8 Fe/Ce/Al samples are quite close (Figure 6). At the same time, the isotopic transient experiment $^{18}O_2/N_2{}^{16}O$ performed on $LaMnO_3$ at 900 °C revealed that there is direct oxygen transfer to the catalysts' bulk from N_2O molecule, and O_2 formed involves lattice oxygen [40]:

$$2N_2{}^{16}O + 2{}^{18}O_{latt} \rightarrow {}^{18}O_2 + 2{}^{16}O_{latt} + 2N_2 \quad (1)$$

This means that catalytic activity should depend on oxygen exchange properties.

In CeO_2-containing compounds a simplified redox scheme realized in Fe oxides or $FeOx/Al_2O_3$ systems:

$$Fe^{2+} + N_2O \rightarrow N_2 + Fe^{3+}\text{-}O \quad (2)$$

$$2Fe^{3+}\text{-}O \leftrightarrow 2Fe^{2+} + O_2 \quad (3)$$

is supplemented by analogous steps for Ce^{3+}/Ce^{4+} redox pair:

$$Ce^{3+} + N_2O \rightarrow N_2 + Ce^{4}\text{-}O \quad (4)$$

$$2Ce^{4+}\text{-}O \leftrightarrow 2Ce^{3+} + O_2 \quad (5)$$

And step corresponding to the additional pathway of oxygen species recombination provided by the presence of neighboring Fe^{3+} and Ce^{4+}:

$$Fe^{3+}O + Ce^{4+}O \leftrightarrow Fe^{2+} + Ce^{3+} + O_2 \quad (6)$$

In addition, reoxidation of Ce^{3+} due to fast oxygen diffusion from CeO_2 lattice (O_{lat}) by extended oxygen vacancies arising after insertion of Fe^{3+} ions into the fluorite lattice:

$$O_{lat} + Ce^{3+} \leftrightarrow Ce^{4+}O \quad (7)$$

Can become an alternative pathway for the supply of the second oxygen atom which is necessary for O_2 desorption and enhancing recombination of oxygen adspecies by steps 2B and 2C without adsorption of the second N_2O molecule. Pure CeO_2 revealed insubstantial activity as related per surface area unit compared with $FeOx/CeO_2$ and even Fe/Al_2O_3 samples [4]. Therefore, the contribution of this pathway is high in Fe/Ce/Al samples containing substantial quantities of both Fe-Ce-O mixed oxide and bulky CeO_2 bonded with FeO_x or Fe-Al-O clusters. Stabilization of a substantial fraction of Ce as isolated Ce^{3+} cations composing mixed Fe-Ce-Al oxides in the Fe/(Ce + Al) samples diminishes substantially the efficiency of oxygen transfer to Fe^{3}-O sites.

3. Materials and Methods

3.1. Catalysts Preparation

Two procedures were used to prepare the supports with a CeO_2:Al_2O_3 weight ratio of 1:1. In the first of them, the precursor of CeO_2 was deposited from 0.75 M $Ce(NO_3)_3 \cdot 6H_2O$ (99.0%, Vekton, Saint-Petersburg, Russia) water solution using 1 M $(NH_4)_2CO_3$ (99.3 %, Vekton, Saint-Petersburg, Russia) as a precipitation agent onto Al_2O_3 (the product of thermochemical activation of hydrargillite calcined at 500 °C) characterized by BET surface area at 210 m^2g^{-1}). After washing by H_2O unless the pH of the filtrate was 7 and drying at 60 °C overnight, the sample was calcined at 900 °C for 5 h and denoted below as Ce/Al. In the second procedure, the water solution of $(NH_4)_2CO_3$ was added dropwise to a water solution of $Al(NO_3)_3 \cdot 9H_2O$ (98.5%, Ecros, Saint-Petersburg, Russia) and $Ce(NO_3)_3 \cdot 6H_2O$ mixed in the necessary proportion unless (Ce + Al)/CO_3 (mole) = 2.5 value was reached. Thus, the obtained gel was dried at 60 °C for 22 h followed by calcination at 500 °C for 2 h and at 900 °C for 5 h resulting in a sample denoted below as (Ce + Al).

FeO_x was supported by incipient wetness impregnation of Ce/Al and (Ce + Al) by water solution of $Fe(NO_3)_3 \cdot 9H_2O$ (98.5%, Vekton, Saint-Petersburg, Russia) with necessary concentration with added citric acid (99.8%, Vekton, Saint-Petersburg, Russia) in 10 wt.% excess to the stoichiometric amount and ethyleneglycole (99.0%, Ecros, Saint-Petersburg, Russia), dried in air at 150 °C for 3 h and then calcined at 900 °C for 4 h. In the commonly used abbreviation n Fe/support, "n" corresponded to Fe weight % concentration in the sample.

3.2. Characterization

XRD patterns were recorded using D8 diffractometer (Bruker, Germany) with CuKα monochromatic radiation. Each sample was scanned in the range of 2θ from 10° to 70° with a step 0.05°. The surface composition of the samples was investigated by X-ray photoelectron spectroscopy (XPS) using spectrometer SPECS (SPECS, Germany) with Al Kα irradiation (hν = 1486.6 eV). The positions of the peaks of Au $4f_{7/2}$ (84.0 eV) and Cu $2p_{3/2}$

(932.67 eV) core levels were used for calibration of the binding energy (BE) scale. In Raman spectroscopy depth of light penetration depends on the wavelength of monochromatic radiation provided by different sources. We believe that green light (514.5 nm line of an Ar^+ laser with 2 mW power reaching the sample) provides information about the structure of preferentially near-surface layers of the samples, while data on the bulk composition are obtained with near-infrared (NIR) radiation at 1064 nm line (provided by an Nd-YAG laser with 100 mW power output) (Bruker Optik GmbH, Ettlingen, Germany). FT-Raman spectra (3700–100 cm^{-1}, 300 scans, resolution 4 cm^{-1}, 180° geometry) were collected using an RFS 100/S spectrometer (Bruker Optik GmbH, Ettlingen, Germany). Horiba Jobin Yvon T64000 spectrometer (HORIBA Scientific, Palaiseau, France) with micro-Raman setup and backscattering geometry for experimental spectra collection was used to measure the Raman spectra. The spectral resolution was not worse than 1.5 cm^{-1}. The detector was a silicon-based CCD matrix, cooled with liquid nitrogen. The band at 520.5 cm^{-1} of Si single crystal was used to calibrate the spectrometer.

The method of differential dissolution phase analysis (DDPA) [41] was used to reveal the composition and, in some cases, morphology and particle depth distribution of the compounds and phases (including X-Ray amorphous ones) formed in the samples. For this about 10 mg of the sample loaded in a quartz microreactor was dissolved in the flow (3.6 mL/min) of water-based solution with the composition changing from HCl (pH = 2) to 3M HCl (with continuous temperature increase from 20 °C to 90 °C), and finally to 3.6 M HF. Compounds dissolving in milder conditions (HCl (pH = 2) and 1–3M HCl) were reasonably supposed to form in the surface layers of the samples. Better crystallized structures, as a rule, dissolve in HF or even remain insoluble. Change of the outlet mixture composition in time was analyzed by ICP AES 262477-364A spectrometer (BAIRD, Zoeterwoude, The Netherlands) using the spectral lines at 238.2, 308.2, and 413.8 nm which are characteristic for Fe, Al and Ce, respectively.

3.3. Kinetic Measurements and Catalytic Tests

For $^{16}O/^{18}O$ exchange experiments, the sample was first heated to 800 °C in 0.58 vol $\%^{16}O_2$ + He flow and kept at this temperature for 30 min. After, this gas mixture was replaced stepwise by the same one containing $^{18}O_2$ and Ar (1 vol.%) as an inert tracer. All responses were analyzed using QMS 200 gas analyzer (Stanford Research Systems, Sunnyvale, USA) as time variation of the ^{18}O atomic fraction in the gas phase $\alpha_g(t) = \frac{(^{16}O^{18}O+2*^{18}O^{18}O)}{2*(^{16}O^{18}O+^{18}O^{18}O+^{16}O^{16}O)}$. Time dependencies of exchanged oxygen for different samples as related to the mass unit (N_O) were calculated using the formulae $N_o(t) = N_A * \frac{2*C_{O2}*U}{g} * \int_0^t (\alpha_g^{input} - \alpha_g)dt$, where α_g^{input}: isotope fraction in the inlet mixture (0.95), C_{O2}: inlet O_2 concentration (mol/mol), U: flow rate of the reaction mixture (mole/s), N_A: Avogadro number. Dynamics of oxygen adsorption/desorption at 800 °C was elucidated from the experiments on the stepwise replacement of He by 0.5 vol.% O_2 + 1 vol.% Ar + He mixture and vice versa flowing the reactor. (O_2 + He)/He switch was performed after at least 30 min sample stay in O_2 containing flow, while He/(O_2 + He) one followed in about 60 s. All kinetic measurements were performed with the sample (*g* = 0.025 g, particles of 250–500 μm in a size) loaded into a reactor (quartz tube, i.d. = 3 mm). The gas flow rates of all mixtures amounted to 16.7 cm^3/s.

The catalytic activity for samples with particles of 250–500 μm in a size was measured in a fixed-bed U-shaped reactor (3 mm i.d. quartz tube) at ambient pressure in the temperature range 700–900 °C. For NH_3 oxidation, mixture 1% NH_3 + 20% O_2 in N_2 was fed to the reactor charged by 0.015 g of the sample with a flow rate of 6.9 cm^3/s. Concentrations of NH_3 and NO_x (x = 0.5–2) in the outlet mixture were measured by infrared spectroscopy. For N_2O decomposition, a gas mixture of 0.15 vol% N_2O in He flowed the reactor charged with 0.038 g of the sample with a flow rate of 16.7 cm^3/s. In some experiments about 3 vol.% O_2 (+3 vol.% H_2O) were added to the inlet mixture. Outlet mixture composition was analyzed by gas chromatograph equipped with Porapack T (i.d. = 3mm, l = 3 m, for N_2O analysis) and NaX (i.d. = 3mm, l = 2 m, for N_2 analysis) columns. N_2O or NH_3

conversion ($X_{N2O(NH3)}$) and yield (Y_i) values calculated as $X_{N2O} = \frac{(C^o_{N_2O} - C_{N_2O})}{C^o_{N_2O}} * 100\%$, $X_{NH3} = \frac{(C^o_{NH_3} - C_{NH_3})}{C^o_{NH_3}} * 100\%$, and $Y_i = \frac{n * C_i}{C^o_{NH_3}} * 100\%$, ($C_i$ and C^o_i: outlet and inlet concentrations of *i*th compound, n: number of N atoms in the *i*th molecule) were considered as a measure of samples activity.

4. Conclusions

FeOx (2.5–9.9 weight.% in terms of Fe) was supported by impregnation of mixed CeO_2-Al_2O_3 support prepared either by co-precipitation (Ce + Al) or CeO_2 precipitation onto Al_2O_3 (Ce/Al). Preferentially Fe-Ce-Al mixed oxides both in the surface layers and in the bulk were formed in Fe/(Ce + Al) samples, while the substantial spatial division of ceria and alumina-based compounds remains intact in Fe/Ce/Al samples. The stabilization of Ce^{3+} in Fe-Ce-Al mixed oxides was shown to inhibit oxygen mobility in the near-surface layers of Fe/(Ce + Al) samples. It results in retardation of the additional pathway of oxygen supply to the sites responsible for O_2 desorption and explains the lower activity of Fe/(Ce + Al) samples in N_2O decomposition.

Supplementary Materials: The following supporting information can be downloaded at: https://www.mdpi.com/article/10.3390/catal12090938/s1, Figure S1: XRD patterns of Ce/Al (A) and (Ce + Al) (B) based samples with different content of Fe, Figure S2: Dependence of N_2O conversion on the temperature for Ce/Al (A) and (Ce + Al) (B) based samples, Figure S3: Effect of O_2 and H_2O presence in the inlet flow on N_2O conversion over 3.8 Fe/Ce/Al and 2.5 Fe/(Ce + Al) samples. T = 800 °C, Figure S4: Temperature dependence of the conversion (A) yield of (NO + NO_2) and N2O (B) at NH_3 oxidation over different Fe/Ce-Al-O based samples. Stability tests for 9.9 Fe/Ce/Al sample (C) at 800 °C, Figure S5: Differential dissolution curves of Ce and Al (A) and identified compounds (B) at stepwise consecutive change of flow composition from HCl (pH = 2) to 1-3M HCl (1) and then to 3.6 M HF (2) over (Ce + Al) sample, Figure S6: Differential dissolution curves of Fe, Ce and Al (A) and identified compounds (B) at stepwise consecutive change of flow composition from HCl (pH = 2) to 1-3M HCl (1) and then to 3.6 M HF (2) over 2.5 Fe/(Ce + Al) sample, Figure S7: Differential dissolution curves of Fe, Ce and Al (A) and initially (B) and finally (C) identified Fe-Ce-Al compounds at stepwise consecutive change of flow composition from HCl (pH = 2) to 1–3M HCl (1) and then to 3.6 M HF (2) over 3.8 Fe/Ce/Al sample; Table S1: Quantity of Fe, Ce, Al (as prepared, dissolved and insoluble) in different samples (mmol/g). Quantities of insoluble compounds were calculated from balance equations.

Author Contributions: Conceptualization, L.P.; investigation, L.P., I.P., Y.C.; writing—original draft preparation, L.P.; visualization, L.P., I.P., Y.C; writing—review and editing L.P., V.A., supervision, L.P., V.A. All authors have read and agreed to the published version of the manuscript.

Funding: This work was supported by the Ministry of Science and Higher Education of the Russian Federation within the governmental order for Boreskov Institute of Catalysis (project AAAA-A21-121011390010-7), granted by the Government of the Russian Federation (075-15-2022-1132).

Acknowledgments: The authors appreciate the performing of DDPA measurements and discussion of the results by Dovlitova L.S.

Conflicts of Interest: The authors declare that they have no known competing interests or personal relationships that could have appeared to influence the work reported in this paper.

References

1. Groves, M.C.E.; Sasonow, A. Uhde EnviNOx® technology for NO_X and N_2O abatement: A contribution to reducing emissions from nitric acid plants. *J. Integr. Environ. Sci.* **2010**, *7*, 211–222. [CrossRef]
2. Pérez-Ramírez, J.; Kapteijn, F.; Schöffel, K.; Moulijn, J.A. Formation and control of N_2O in nitric acid production. Where do we stand today? *Appl. Catal. B Environ.* **2003**, *44*, 117–151. [CrossRef]
3. Sadykov, V.A.; Isupova, L.A.; Zolotarskii, I.A.; Bobrova, L.N.; Noskov, A.S.; Parmon, V.N.; Brushtein, E.A.; Telyatnikova, T.V.; Chernyshev, V.I.; Lunin, V.V. Oxide catalysts for ammonia oxidation in nitric acid production: Properties and perspectives. *Appl. Catal. A Chem.* **2000**, *204*, 59–87. [CrossRef]

4. Pinaeva, L.G.; Prosvirin, I.P.; Dovlitova, L.S.; Danilova, I.G.; Sadovskaya, E.M.; Isupova, L.A. MeO_x/Al_2O_3 and MeO_x/CeO_2 (Me = Fe, Co, Ni) catalysts for high temperature N_2O decomposition and NH_3 oxidation. *Catal. Sci. Technol.* **2016**, *6*, 2150–2161. [CrossRef]
5. Pinaeva, L.G.; Dovlitova, L.S.; Isupova, L.A. Monolithic FeO_x/Al_2O_3 Catalysts for Ammonia Oxidation and Nitrous Oxide Decomposition. *Kinet. Catal.* **2017**, *58*, 167–178. [CrossRef]
6. Giecko, G.; Borowiecki, T.; Gac, W.; Kruk, J. Fe_2O_3/Al_2O_3 catalysts for the N_2O decomposition in the nitric acid industry. *Catal. Today* **2008**, *137*, 403–409. [CrossRef]
7. Kruk, J.; Stołecki, K.; Michalska, K.; Konkol, M.; Kowalik, P. The influence of modifiers on the activity of Fe_2O_3 catalyst for high temperature N_2O decomposition (HT-deN_2O). *Catal. Today* **2012**, *191*, 125–128. [CrossRef]
8. Sádovská, G.; Tabor, E.; Bernauer, M.; Sazama, P.; Fíla, V.; Kmječ, T.; Kohout, J.; Závěta, K.; Tokarová, V.; Sobalík, Z. FeOx/Al_2O_3 catalysts for high-temperature decomposition of N_2O under conditions of NH_3 oxidation in nitric acid production. *Catal. Sci. Technol.* **2018**, *8*, 2841–2852. [CrossRef]
9. Imagawa, H.; Suda, A.; Yamamura, K.; Sun, S. Monodisperse CeO_2 Nanoparticles and Their Oxygen Storage and Release Properties. *J. Phys. Chem. C* **2011**, *115*, 1740–1745. [CrossRef]
10. Chen, L.; Fleming, P.; Morris, V.; Holmes, J.D.; Morris, M.A. Size-Related Lattice Parameter Changes and Surface Defects in Ceria Nanocrystals. *J. Phys. Chem. C* **2010**, *114*, 12909–12919. [CrossRef]
11. Iwanek, E.; Krawczyk, K.; Petryk, J.; Sobczak, J.W.; Kaszkur, Z. Direct nitrous oxide decomposition with CoOx-CeO_2 catalysts. *Appl. Catal. B Environ.* **2011**, *106*, 416–422. [CrossRef]
12. Grzybek, G.; Stelmachowski, P.; Gudyka, S.; Indyka, P.; Sojka, Z.; Guillén-Hurtado, N.; Rico-Pérez, V.; Bueno-López, A.; Kotarba, A. Strong dispersion effect of cobalt spinel active phase spread over ceria for catalytic N_2O decomposition: The role of the interface periphery. *Appl. Catal. B Environ.* **2016**, *180*, 622–629. [CrossRef]
13. Ferreira, A.P.; Zanchet, D.; Rinaldi, R.; Schuchardt, U.; Damyanova, S.; Bueno, J.M.C. Effect of the CeO_2 content on the surface and structural properties of CeO_2–Al_2O_3 mixed oxides prepared by sol–gel method. *Appl. Catal. A Chem.* **2010**, *388*, 45–56. [CrossRef]
14. Damyanova, S.; Perez, C.A.; Schmal, M.; Bueno, J.M.C. Characterization of ceria-coated alumina carrier. *Appl. Catal. A Chem.* **2002**, *234*, 271–282. [CrossRef]
15. Boullosa-Eiras, S.; Vanhaecke, E.; Zhao, T.; Chen, D.; Holmen, A. Raman spectroscopy and X-ray diffraction study of the phase transformation of ZrO_2–Al_2O_3 and CeO_2–Al_2O_3 nanocomposites. *Catal. Today* **2011**, *166*, 10–17. [CrossRef]
16. Ge, C.; Liu, L.; Liu, Z.; Yao, X.; Cao, Y.; Tang, C.; Gao, F.; Dong, L. Improving the dispersion of CeO_2 on γ-Al_2O_3 to enhance the catalytic performances of $CuO/CeO_2/\gamma$-Al_2O_3 catalysts for NO removal by CO. *Catal. Commun.* **2014**, *51*, 95–99. [CrossRef]
17. Laguna, O.H.; Romero Sarria, F.; Centeno, M.A.; Odriozola, J.A. Gold supported on metal-doped ceria catalysts (M = Zr, Zn and Fe) for the preferential oxidation of CO (PROX). *J. Catal.* **2010**, *276*, 360–370. [CrossRef]
18. Zhang, Z.; Han, D.; Wei, S.; Zhang, Y. Determination of active site densities and mechanisms for soot combustion with O_2 on Fe-doped CeO_2 mixed oxides. *J. Catal.* **2010**, *276*, 16–23. [CrossRef]
19. Li, K.; Wang, H.; Wei, Y.; Yan, D. Direct conversion of methane to synthesis gas using lattice oxygen of CeO_2–Fe_2O_3 complex oxides. *Chem. Eng. J.* **2010**, *156*, 512–518. [CrossRef]
20. Gupta, A.; Kumar, A.; Waghmare, U.V.; Hegde, M.S. Origin of activation of Lattice Oxygen and Synergistic Interaction in Bimetal-Ionic $Ce_{0.89}Fe_{0.1}Pd_{0.01}O_{2-\delta}$ Catalyst. *Chem. Mater.* **2009**, *21*, 4880–4891. [CrossRef]
21. Escribano, V.S.; Amores, J.M.G.; Finocchio, E.; Daturi, M.; Busca, G. Characterization of α-$(Fe,Al)_2O_3$ solid-solution powders. *J. Mater. Chem.* **1995**, *5*, 1943–1951. [CrossRef]
22. McBride, J.R.; Hass, K.C.; Poindexter, B.D.; Weber, W.H. Raman and x-ray studies of $Ce_{1-x}RE_XO_{2-y}$ where RE=La, Pr, Nd, Eu, Gd, and Tb. *J. Appl. Phys.* **1994**, *76*, 2435–2441. [CrossRef]
23. Kosacki, I.; Suzuki, T.; Anderson, H.U.; Colomban, P. Raman scattering and lattice defects in nanocrystalline CeO_2 thin films. *Solid State Ion.* **2002**, *149*, 99–105. [CrossRef]
24. Spanier, J.E.; Robinson, R.D.; Zhang, F.; Chan, S.W.; Herman, I.P. Size-dependent properties of CeO_{2-y} nanoparticles as studied by Raman scattering. *Phys. Rev. B* **2001**, *64*, 245407. [CrossRef]
25. Tsunekawa, S.; Ishikawa, K.; Li, Z.Q.; Kawazoe, Y.; Kasuya, Y. Origin of Anomalous Lattice Expansion in Oxide Nanoparticles. *Phys. Rev. Lett.* **2000**, *85*, 3440–3443. [CrossRef] [PubMed]
26. Ojha, A.K.; Ponnilavan, V.; Kannan, S. Structural, morphological and mechanical investigations of in situ synthesized c-CeO_2/α-Al_2O_3 composites. *Ceram. Int.* **2017**, *43*, 686–692. [CrossRef]
27. Porto, S.P.S.; Krishnan, R.S. Raman Effect of Corundum. *J. Chem. Phys.* **1967**, *47*, 1009–1012. [CrossRef]
28. Sudarsanama, P.; Malleshama, B.; Reddy, P.S.; Großmann, D.; Grünert, W.; Reddy, B.M. Nano-Au/CeO_2 catalysts for CO oxidation: Influence of dopants (Fe, La and Zr) on the physicochemical properties and catalytic activity. *Appl. Catal. B Environ.* **2014**, *144*, 900–908. [CrossRef]
29. Schilling, C.; Hofmann, A.; Hess, C.; Ganduglia-Pirovano, M.V. Raman Spectra of Polycrystalline CeO_2: A Density Functional Theory Study. *J. Phys. Chem. C* **2017**, *121*, 20834–20849. [CrossRef]
30. Reina, T.R.; Ivanova, S.; Centeno, M.A.; Odriozola, J.A. Boosting the activity of a Au/CeO_2/Al_2O_3 catalyst for the WGS reaction. *Catal. Today* **2015**, *253*, 149–154. [CrossRef]
31. Laguna, O.H.; Centeno, M.A.; Boutonnet, M.; Odriozola, J.A. Fe-doped ceria solids synthesized by the microemulsion method for CO oxidation reactions. *Appl. Catal. B Environ.* **2011**, *106*, 621–629. [CrossRef]

32. Perez-Alonso, F.J.; Melián-Cabrera, I.; López Granados, M.; Kapteijn, F.; Fierro, J.L.G. Synergy of $Fe_xCe_{1-x}O_2$ mixed oxides for N_2O decomposition. *J. Catal.* **2006**, *239*, 340–346. [CrossRef]
33. Suzuki, S.; Yanagihara, K.; Hirokawa, K. XPS study of oxides formed on the surface of high-purity iron exposed to air. *Surf. Interface Anal.* **2000**, *30*, 372–376. [CrossRef]
34. Grosvenor, A.P.; Kobe, B.A.; Biesinger, M.C.; McIntyre, N.S. Investigation of multiplet splitting of Fe 2p XPS spectra and bonding in iron compounds. *Surf. Interface Anal.* **2004**, *36*, 1564–1574. [CrossRef]
35. Atuchin, V.V.; Vinnik, D.A.; Gavrilova, T.A.; Gudkova, S.A.; Isaenko, L.I.; Jiang, X.; Pokrovsky, L.D.; Prosvirin, I.P.; Mashkovtseva, L.S.; Lin, Z. Flux Crystal Growth and the Electronic Structure of $BaFe_{12}O_{19}$ Hexaferrite. *J. Phys. Chem. C* **2016**, *120*, 5114–5123. [CrossRef]
36. Yamashita, T.; Hayes, P. Analysis of XPS spectra of Fe^{2+} and Fe^{3+} ions in oxide materials. *Appl. Surf. Sci.* **2008**, *254*, 2441–2449. [CrossRef]
37. Merte, L.R.; Gustafson, J.; Shipilin, M.; Zhang, C.; Lundgren, E. Redox behavior of iron at the surface of an $Fe_{0.01}Mg_{0.99}O(100)$ single crystal studied by ambient-pressure photoelectron spectroscopy. *Catal. Struct. React.* **2017**, *3*, 95–103.
38. Sayed, F.N.; Polshettiwar, V. Facile and sustainable synthesis of shaped iron oxide nanoparticles: Effect of iron precursor salts on the shapes of iron oxides. *Sci. Rep.* **2015**, *5*, 09733. [CrossRef]
39. Kapteijn, F.; Rodriguez-Mirasol, J.; Moulijn, J. Heterogeneous catalytic decomposition of nitrous oxide. *Appl. Catal. B Environ.* **1996**, *9*, 25–64. [CrossRef]
40. Ivanov, D.V.; Pinaeva, L.G.; Sadovskaya, E.M.; Isupova, L.A. Isotopic transient kinetic study of N_2O decomposition on $LaMnO_{3+\delta}$. *J. Mol. Catal. A Chem.* **2016**, *412*, 34–38. [CrossRef]
41. Malakhov, V.; Boldyreva, N.; Vlasov, A.; Dovlitova, L. Methodology and procedure of the stoichiographic analysis of solid inorganic substances and materials. *J. Analyt. Chem.* **2011**, *66*, 458–464. [CrossRef]